 doi:10.20944/preprints202009.0017.v1

Article

Addressed Fiber Bragg Structures in Load Sensing Wheel Hub Bearings

Timur Agliullin[1*], Robert Gubaidullin[1], Airat Sakhabutdinov[1], Oleg Morozov[1], Artem Kuznetsov[1], Valentin Ivanov[2]

[1] Kazan National Research Technical University named after A.N. Tupolev-KAI; microoil@mail.ru
[2] Automotive Engineering Group, Technische Universität Ilmenau; valentin.ivanov@tu-ilmenau.de
* Correspondence: taagliullin@mail.ru

Received: date; Accepted: date; Published: date

Abstract: The work presents an approach to instrument the load sensing bearings for automotive applications for estimation of the loads acting on the wheels. The system comprises fiber-optic sensors based on addressed fiber Bragg structures (AFBS) with two symmetrical phase shifts. A mathematical model for load-deformation relation is presented, and the AFBS interrogation principle is described. The simulation includes (i) modeling of vehicle dynamics in a split-mu braking test, during which the longitudinal wheel loads are obtained, (ii) the subsequent estimation of bearing outer ring deformation using a beam model with simply supported boundary conditions, (iii) the conversion of strain into central wavelength shift of AFBS, and (iv) modeling of the beating signal at the photodetector. The simulation results show that the estimation error of the longitudinal wheel force from the strain data acquired from a single measurement point was 5.44% with root-mean-square error of 113.64 N. A prototype load sensing bearing was instrumented with a single AFBS sensor and mounted in a front right wheel hub of an experimental vehicle. The experimental setup demonstrated comparable results with the simulation during the braking test. The proposed system with load-sensing bearings is aimed at estimation of the loads acting on the wheels, which serve as input parameters for active safety systems, such as automatic braking, adaptive cruise control, or fully automated driving, in order to enhance their effectiveness and safety of the vehicle.

Keywords: microwave photonic sensor system; numerical simulation; addressed fiber Bragg structures; load sensing bearings; vehicle dynamics control

1. Introduction

Various active safety systems such as anti-lock braking system (ABS) and electronic stability control (ESC) have been used to increase driving safety for several decades [1, 2]. However, their efficiency depends on the correctness of tire-road traction parameters that are currently estimated by means of indirect methods [3, 4], which do not always provide sufficient accuracy, therefore limiting the capabilities of such systems for vehicle dynamics control.

In order to mitigate this issue, a significant research effort is aimed at the development of the corresponding direct methods, in particular, based on the real-time measurement of loads acting on the wheels, using a variety of sensor types. Theoretically, every component of the vehicle transferring the loads from the tire contact patch to vehicle body can be used to estimate the wheel loads. Thus four main categories of wheel force determination methods can be distinguished in accordance with the vehicle components they are based on: tire-based methods (including the ones that use piezoelectric [5–7], fiber-optic [8–10], optical [11–13] sensors, electrical resistant strain gauges [14, 15], as well as accelerometers [16]); wheel disc-based methods (primarily used in testing equipment [7]); suspension-based methods (including strain measurement of suspension bushings [17], displacement measurement of knuckle [18]), and wheel hub bearings-based methods (load

Preprints (www.preprints.org) | NOT PEER-REVIEWED | Posted: 1 September 2020 doi:10.20944/preprints202009.0017.v1

sensing bearings) [19–22, 24, 31]. Wheel forces measurement based on load sensing hub bearings has a number of advantages in comparison with the other approaches. Firstly, the sensors are located on a non-rotating ring of the bearing, therefore significantly simplifying data acquisition. Secondly, the hub bearings generally have much longer lifespan than tires. Thirdly, the methods based on load sensing bearings are robust in case of tire or wheel change. Finally, load sensing hub bearings are located closer to the contact patch than other suspension components, therefore providing more precise load estimation.

2. Load Sensing Bearings in Automotive Applications

Figure 1 illustrates the dependence of wheel loads on road conditions by presenting examples of the longitudinal wheel force as the function of the wheel slip ratio k for various conditions of the road surface [23]. As it can be seen from the figure, the magnitude of the wheel force varies for different road conditions in the wide range.

The wheel slip ratio k is defined using the expression (1) in case of braking, and using the expression (2) in case of acceleration:

$$k = \frac{v_x - \omega_w r_w}{v_x}, \tag{1}$$

$$k = \frac{\omega_w r_w - v_x}{\omega_w r_w}, \tag{2}$$

where v_x is the vehicle longitudinal velocity, ω_w is the angular velocity of the wheel, r_w is the dynamic radius of the wheel.

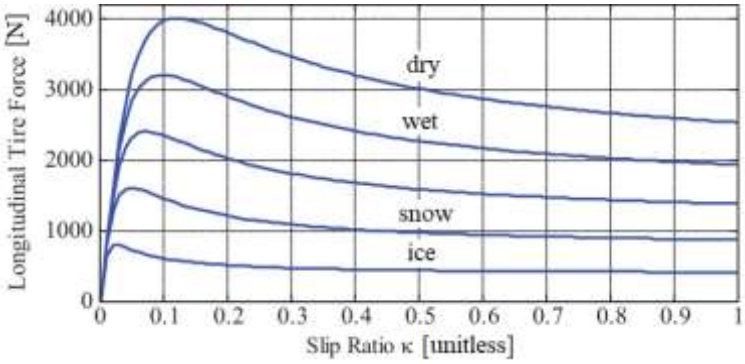

Figure 1. Longitudinal wheel force as the function of wheel slip ratio for various road conditions [23].

As it can be seen from Figure 1, the longitudinal wheel force reaches the maximum value at a certain wheel slip ratio, which stands for the most efficient braking or acceleration. It must be noted that the wheel slip corresponding to the maximum wheel force is different for various road conditions, which further complicates its indirect estimation. During acceleration or braking, the load sensing bearings detect the peak wheel force, and the slip ratio is adjusted to maintain the peak value in order to provide the most effective interaction between the wheels and road. It should be noted that some low-friction roads as well as deformable surfaces have no clearly pronounced extremum of the longitudinal force-slip-curve. In this case the analysis of the curve slope should be considered by seeking the peak value. However, the presented paper does not include case studies with such surfaces.

In this work, we consider wheel hub bearings with non-rotating outer rings. The load applied to the inner ring of the bearing is translated to the outer ring via rolling elements (balls) and causes strain of the outer ring. This tangential deformation measured by a single sensor has a periodic sinusoidal behavior even at constant loading due to the movement of the rolling elements. Thus, the maximum strain is registered when the ball position coincides with the location of the sensor, and

 doi:10.20944/preprints202009.0017.v1

the minimal strain is achieved when the sensor is located in the middle between two adjacent rolling elements [22] (see Figure 2, where P_r is the radial load applied to the inner ring of the bearing).

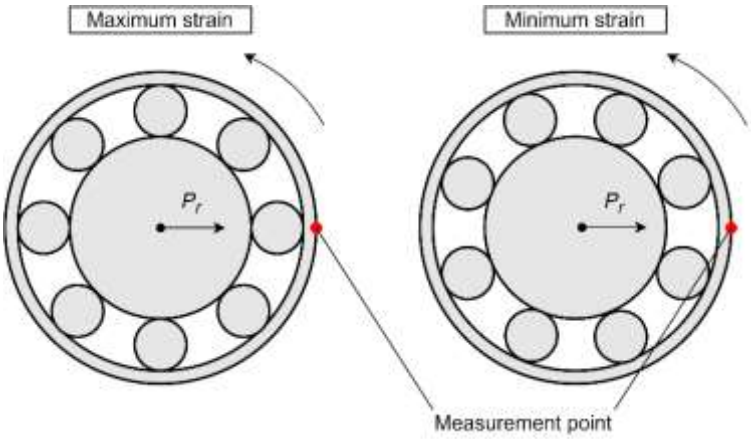

Figure 2. Position of the sensor relative to the rolling elements at maximum and minimum of measured strain.

The current work proposes the usage of fiber-optic sensors for strain measurement of bearing outer ring. With all the intrinsic advantages of fiber-optic sensors based on fiber Bragg gratings (FBG), such as low weight, small footprint, immunity to electromagnetic interference, absence of electric power supply, a significant disadvantage still persists that is related to the usage of electro-optic interrogators. The complexity and high cost of such devices, which are designed to define the FBG central wavelength by scanning its spectral response, constrain the areas of application of FBG-based sensor systems [26, 35].

In order to solve the abovementioned issue, the addressed fiber Bragg structures (AFBS) have been developed [27–34] and further expanded into multi-addressed fiber Bragg structures [35]. Two approaches for AFBS design have been proposed to date: 2λ-FBG and 2π-FBG. The 2λ-FBG is based on two sequentially formed ultra-narrowband FBGs with different Bragg wavelengths [32, 33]. An addressed structure with two symmetrical π-phase shifts (2π-FBG) consists of three FBGs divided by the discrete symmetrical phase shifts [27, 29–31, 34]. 2π-FBGs are generally shorter in comparison with 2λ-FBGs, which makes them more suitable for applications where minimal sensor length is required, for instance, in load sensing bearings due to their relatively small diameter [32]. The system can include several AFBSs with the same Bragg wavelength, and the sensors are distinguished using their address frequencies, which are unique for each sensor in the system. The address frequency is defined as the frequency spacing between the two transparency windows in the AFBS spectral response, which does not change when the structure is subjected to strain or temperature fields.

3. AFBS Interrogation Principle

Figure 3 presents the optic-electrical scheme of the interrogation system for two AFBSs of 2π-FBG-type. A broadband light source (1) generates continuous light radiation (diagram a), which corresponds to the measurement bandwidth. The light passes through a fiber-optic splitter (9) and enters the 2π-FBG-sensors (2.1 and 2.2), both of which form two-frequency radiations that are merged into a four-frequency optical response (diagrams b, c) by a fiber-optic coupler (10). After that, a fiber-optic splitter (6) divides the optical signal into two channels – the measuring channel and the reference channel. In the measuring channel, an optical filter (3) with a predefined linear inclined frequency response is installed, which modifies the amplitudes of the two-frequency radiation into the asymmetrical radiation (diagram d). After that, the signal is sent to the photodetector (4) and is received by the measuring analog-to-digital converter (ADC) (5). The signal from the ADC (5) is used to define the measurement information from the AFBS. In the reference

Preprints (www.preprints.org) | NOT PEER-REVIEWED | Posted: 1 September 2020 doi:10.20944/preprints202009.0017.v1

channel, the unmodified signal (diagram e) is sent to the reference photodetector (7) and then it is processed by the reference ADC (8). All the subsequent calculations are performed using the relations of the signal amplitudes in the measuring and reference channels. Therefore, the normalization of output signal intensity is achieved, eliminating the influence of the light source power fluctuations on the amplitudes of the AFBSs optical spectrum response.

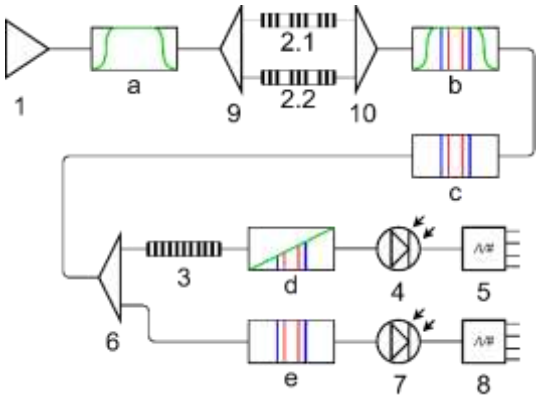

Figure 3. Structure of the interrogation system for two AFBS-based sensors.

The optical response from the *i*-th AFBS is represented as follows:

$$E_i(t) = A_i e^{j\omega_i t + \varphi_{Ai}} + B_i e^{j(\omega_i + \Omega_i)t + \varphi_{Bi}}, \quad (3)$$

where A_i, B_i are the amplitudes of the AFBS spectral components; ω_i is the frequency of the left spectral component of the *i*-th AFBS; Ω_i is the address frequency, φ_{Ai}, φ_{Bi} are phases. It must be noted that the proposed mathematical representation of AFBS spectrum does not take into account the spectral shape of the transparency windows, which can be described using the Gaussian (in case of 2λ-FBG [33]) or Lorentz (in case of 2π-FBG [34]) functions.

The luminous power received by the photodetector from *N* addressed structures can be described using the expression (4) by multiplying the expression (3) with its complex conjugate:

$$\begin{aligned} P(t) &= \left(\sum_{i=1}^{N} E_i(t)\right)\left(\overline{\sum_{i=1}^{N} E_i(t)}\right) = \left(\sum_{i=1}^{N}\left(A_i e^{j\omega_i t + \varphi_{Ai}} + B_i e^{j(\omega_i + \Omega_i)t + \varphi_{Bi}}\right)\right)\left(\sum_{k=1}^{N}\left(A_k e^{-(j\omega_k t + \varphi_{Ak})} + B_k e^{-(j(\omega_k + \Omega_k)t + \varphi_{Bk})}\right)\right) = \\ &= \sum_{i=1}^{N}(A_i^2 + B_i^2) + 2\sum_{i=1}^{N} A_i B_i \cos(\Omega_i t + \varphi_{Ai} - \varphi_{Bi}) + \\ &+ 2\sum_{i=1}^{N}\sum_{k=i+1}^{N}\begin{pmatrix} A_i A_k \cos((\omega_i - \omega_k)t + \varphi_{Ai} - \varphi_{Ak}) + \\ A_i B_k \cos((\omega_i - \omega_k - \Omega_k)t + \varphi_{Ai} - \varphi_{Bk}) + \\ B_i A_k \cos((\omega_i - \omega_k + \Omega_i)t + \varphi_{Bi} - \varphi_{Ak}) + \\ B_i B_k \cos((\omega_i - \omega_k + \Omega_i - \Omega_k)t + \varphi_{Bi} - \varphi_{Bk}) \end{pmatrix}. \end{aligned} \quad (4)$$

As it can be seen, the oscillation of output electric signal of the photodetector at the address frequency Ω_i is proportional to the amplitudes of the AFBS optical spectral components A_i and B_i. The amplitudes A_i and B_i are defined by the parameters *u* and *v* of the linear function describing the frequency response of the optical filter with inclined frequency response ((3) in Figure 3):

$$A_i = L_0(u\omega_i + v),\ B_i = L_0(u(\omega_i + \Omega_i) + v), \quad (5)$$

where *u* is the slope ratio, *v* is the free term of the equation describing the frequency response of the optical filter, L_0 is the amplitude of the optical spectral component of the AFBS prior to entering the filter with inclined linear frequency response. By measuring the amplitude of the photodetector output signal at the address frequency Ω_i, it is possible to define the central wavelength shift (or the frequency of the left spectral component ω_i) of the AFBS. However, due to the appearance of the

Preprints (www.preprints.org) | NOT PEER-REVIEWED | Posted: 1 September 2020 doi:10.20944/preprints202009.0017.v1

additional frequency components in the last sum of the expression (4), the filtering of signal at the address frequencies is required.

4. Modeling of Vehicle Dynamics

As it was mentioned before, load sensing bearings are used to assess the tire-road friction characteristics based on the wheel forces. In order to define the forces acting on the wheels in various conditions, consider a split-mu braking test, which was simulated using the CarSim software. A split-mu braking test is a common vehicle testing procedure that presupposes straight braking in a lane with significantly different frictional coefficients for the left and the right wheel paths. The visualization of the maneuver is shown in Figure 4 (a).

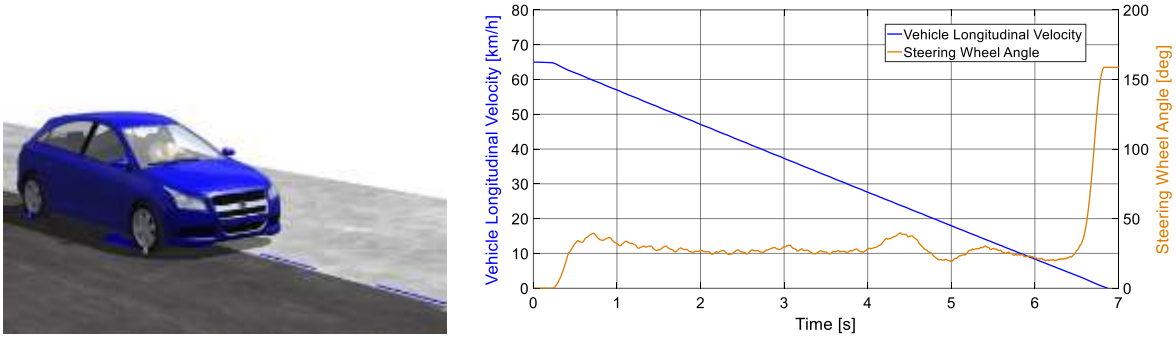

Figure 4. (**a**) Visualization of the split-mu braking test; (**b**) Vehicle longitudinal velocity (blue line) and steering wheel angle (orange line) during the split-mu braking test.

The vehicle under test was a generic C-class hatchback with the following main parameters: sprung mass of 1270 kg, tire size of 215/55 R17, generic braking system with ABS. The friction of the left side of the road was $\mu_L = 0.2$, and the friction of the right side was $\mu_R = 0.5$, which imitates the possible road conditions at low temperatures. The maneuver included braking from the initial velocity of 65 km/h to a standstill with the constant pressure applied to the brake master cylinder of 15 MPa. The ABS was activated during the test in order to eliminate skidding. The profiles of the vehicle longitudinal velocity and steering wheel angle are presented in Figure 4 (b). As it can be seen, the virtual driver applied a certain steering input in order to compensate the yaw moment generated due to the inequality of left and right wheel forces.

The longitudinal wheel forces obtained from the simulation during the split-mu braking test are presented in Figure 5. Using these values, the corresponding deformation of the hub bearing outer ring is calculated, which is described in the next chapter.

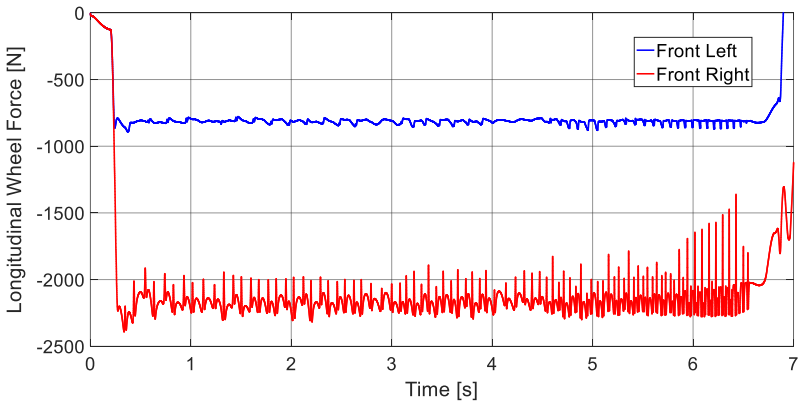

Figure 5. Longitudinal force of the front left wheel (blue line) and front right wheel (red line) during the split-mu braking test.

Preprints (www.preprints.org) | NOT PEER-REVIEWED | Posted: 1 September 2020 doi:10.20944/preprints202009.0017.v1

5. Modeling of Bearing Outer Ring Deformation

In order to estimate tangential deformation of the outer ring of the load sensing bearing caused by the loads acting on the wheels during the maneuver, consider a beam model with simply supported boundary conditions [24]. The model provides a sufficient accuracy for preliminary estimations while maintaining simplicity of calculations [24]. A schematic representation of the beam model is shown in Figure 6, where the following denotations are used: P is the load transmitted to the outer ring by a ball, P_r is the radial load applied to the inner ring of the bearing, x is the position of the sensor (i.e. it is the point, in which the strain is estimated), a and b are the load positions relative to the left end and the right end of the beam, respectively.

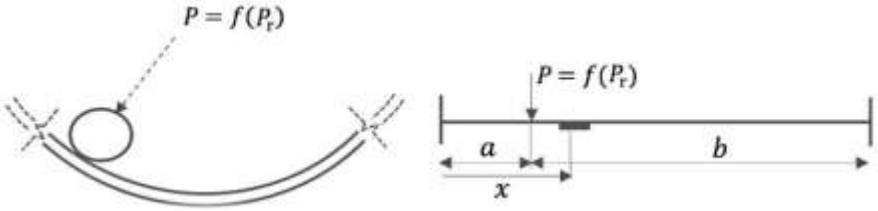

Figure 6. Beam model for a single load case for estimation of the bearing outer ring deformation [22].

As it was mentioned in Chapter 2, the strain of outer ring measured by a single sensor is periodic due to the passage of rolling elements. The maximum values of strain are achieved when the position of the ball coincides with the position of the sensor, and the sensor is located in the middle of a beam, i.e. $a = b = x$, while the minimum strain is detected when the sensor is positioned in the middle between two adjacent balls, i.e. $x - a = \beta/2$, where β is the arc length between the positions of two subsequent balls. In order to define the load applied by the rolling element to the beam, we use a generally accepted relation found by Stribeck in 1900, according to which the load on the most loaded element is 4.37 higher than the average load distributed on the bearing balls [25]:

$$P = 4.37\frac{P_r}{n}, \tag{6}$$

where n is the number of balls in a single row of a bearing.

A single load acting on the bearing ball in a beam model with simply supported boundary conditions is expressed as follows [24]:

$$P = -\frac{L}{bx}\frac{S_x EI}{y}, \tag{7}$$

where S_x is tangential strain at 'x' distance from the left end of a beam; E is Young's modulus; I is the area moment of inertia of a cross-section of the beam; y is distance from neutral axis, where the strain is calculated (i.e. half of the outer ring thickness); $L = a + b$ is the beam length (i.e. half of the perimeter of the outer ring circumference).

Considering $a = b = x = L/2$ for the maximum case, and $x = L/2$, $b = L/2 - L/n$ for the minimum case, the corresponding values of strain can be estimated based on the expression (7):

$$S_{x,\max} = -\frac{(L/2)^2}{L}\frac{yP}{EI}, \tag{8}$$

$$S_{x,\min} = -\frac{(n-2)L}{4n}\frac{yP}{EI}. \tag{9}$$

Using the expressions (8) and (9), the tangential deformation of the bearing outer ring was calculated for the whole duration of the maneuver. The results are presented in Figure 7 (a) for the whole duration of the simulated testing procedure, and in Figure 7 (b) for a shorter time interval. As it can be seen from the figure, the sensor on the front right hub bearing is subjected to significantly

Preprints (www.preprints.org) | NOT PEER-REVIEWED | Posted: 1 September 2020 doi:10.20944/preprints202009.0017.v1

higher strain in comparison with the left one due to higher loads acting on the right wheel caused by higher road traction.

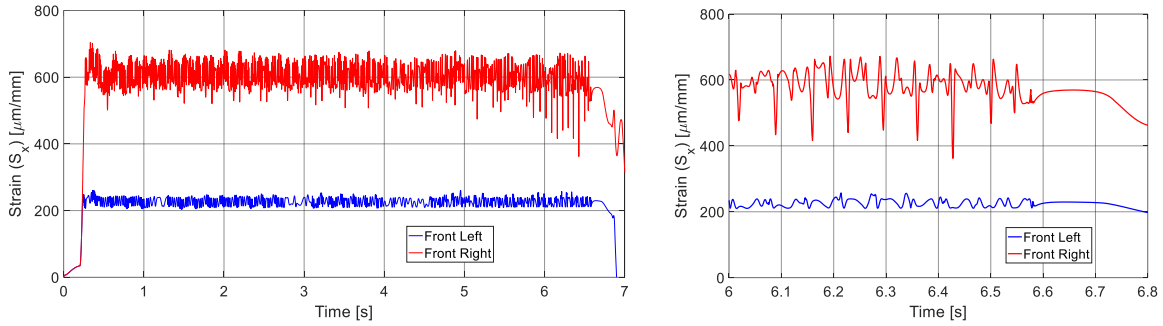

Figure 7. Strain simulated for the front left wheel hub bearing (blue line) and front right wheel hub bearing (red line): (**a**) for the whole duration of the split-mu braking test; (**b**) for t = [6, 6.8] s.

A system based on load sensing bearings is aimed at solving the inverse problem, i.e. the calculation of force using the measured values of strain. In order to assess the estimation accuracy for a system with a single strain sensor, an upper envelope of the simulated strain was obtained for the front right wheel hub of the simulated vehicle, which is shown in Figure 8 (a). After that, the longitudinal wheel force was estimated using the expressions (6) and (7) considering only the maximum strain case. The results are illustrated in Figure 8 (b), while the estimation error found as the difference between simulated and estimated forces is presented in Figure 8 (c). The high overshoot of error at the beginning of simulation results from linear interpolation of strain due to relatively long time interval as well as rapid strain raise between the subsequent strain peaks. The root-mean-square error for the whole duration of the simulation was 113.64 N, which is 5.44 % from the average force of 2087.15 N.

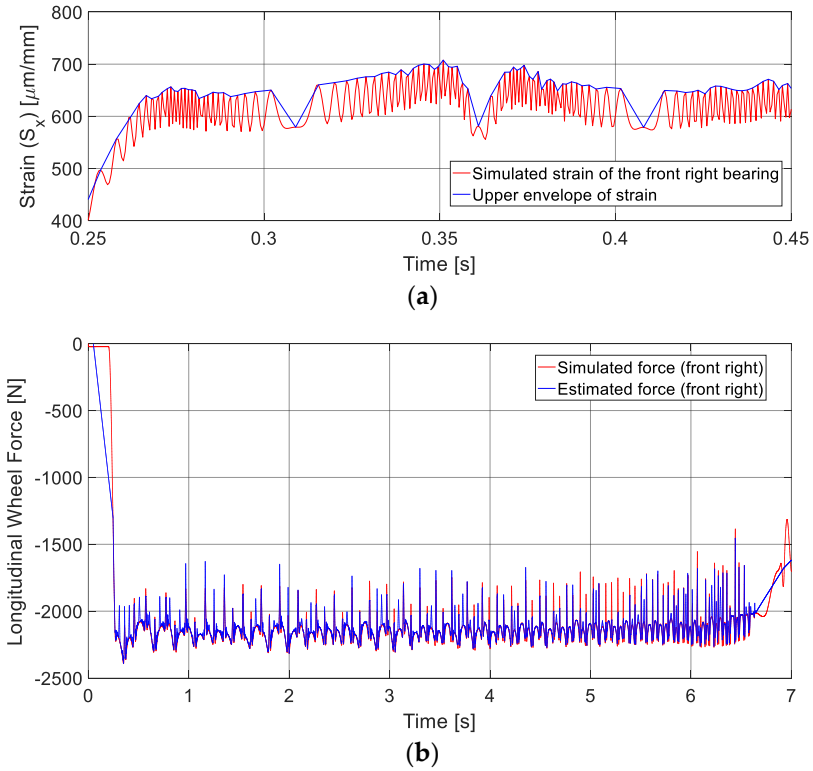

Figure 8. *Cont.*

Preprints (www.preprints.org) | NOT PEER-REVIEWED | Posted: 1 September 2020 doi:10.20944/preprints202009.0017.v1

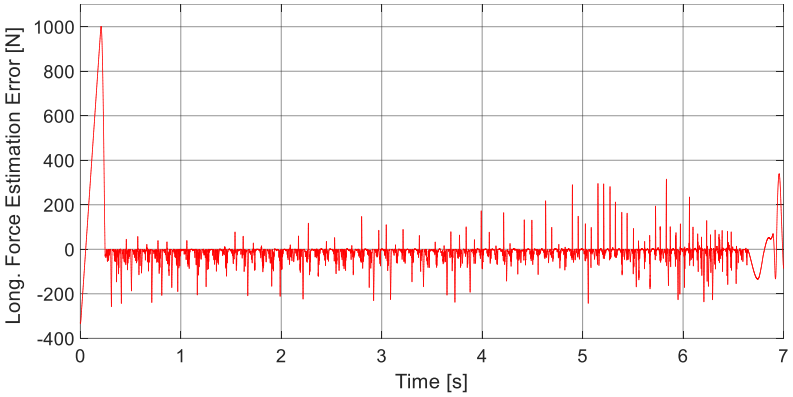

(**c**)

Figure 8. Assessment of the force estimation accuracy by solving the inverse problem: (**a**) strain simulated for the front right hub bearing (red line) and its upper envelope (blue line) shown for a short time interval; (**b**) longitudinal wheel force obtained from the simulation (red line) and estimated force (blue line) for the whole duration of the maneuver; (**c**) force estimation error.

6. Modeling of AFBS Interrogation

Consider a 2π-FBG structure with the address frequency Ω = 3.75 GHz as the sensing element for strain measurement of the bearing outer ring. The simulations of this chapter were performed using the OptiSystem 7.0 software. The optoelectronic interrogation scheme implemented for the simulation is shown in Figure 9. The model does not include the reference channel shown in Figure 3, since the optical source is ideal and does not induce fluctuations of signal intensity. The AFBS spectrum was obtained using the OptiGrating software, the left slope of the frequency response of trapezoidal optical filter with the central wavelength of 1551.6 nm and bandwidth of 1.1 nm was utilized as a filter with inclined frequency response. The abovementioned filter parameters provide a linear frequency response of the filter in the whole range of AFBS sensor wavelength.

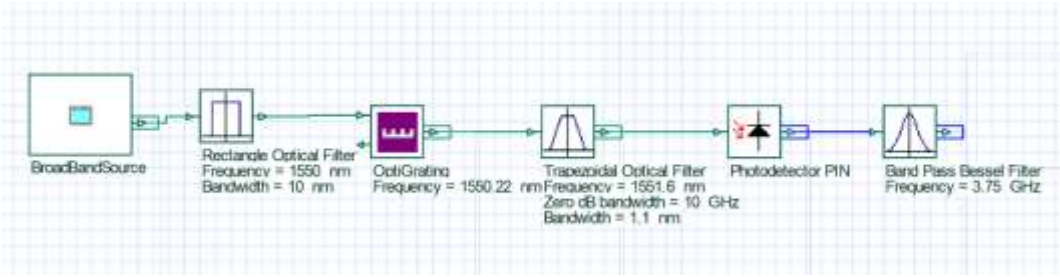

Figure 9. Simulation of the optoelectronic interrogation scheme in the OptiSystem software.

It is known that the central wavelength shift of AFBS, similarly to conventional FBG, depends both on the applied strain and temperature. According to [36], the strain measurement can be represented as a function of the central wavelength shift for the strain sensor and the temperature sensor:

$$\begin{aligned} f(\Delta\lambda_T,\Delta\lambda_P) = c_{2,3}\cdot\Delta\lambda_T^2\cdot\Delta\lambda_P^3 + c_{2,2}\cdot\Delta\lambda_T^2\cdot\Delta\lambda_P^2 + c_{2,1}\cdot\Delta\lambda_T^2\cdot\Delta\lambda_P + \\ + c_{2,0}\cdot\Delta\lambda_T + c_{1,2}\cdot\Delta\lambda_T\cdot\Delta\lambda_P^2 + c_{1,1}\cdot\Delta\lambda_T\cdot\Delta\lambda_P^2 + c_{1,1}\cdot\Delta\lambda_T\cdot\Delta\lambda_P + \\ + c_{1,0}\cdot\Delta\lambda_T + c_{3,0}\cdot\Delta\lambda_P^3 + c_{2,0}\cdot\Delta\lambda^2 + c_{0,1}\cdot\Delta\lambda_P + c_{0,0}, \end{aligned} \quad (10)$$

where $\Delta\lambda_P$ is the shift of the central wavelength due to the deformation, $\Delta\lambda_T$ is the shift of the central wavelength due to temperature exposure, $c_{i,j}$ are calibration coefficients.

In the current simulation, the temperature of the sensor is assumed to be constant and its influence on the central wavelength shift is neglected. The software used for modeling of vehicle

Preprints (www.preprints.org) | NOT PEER-REVIEWED | Posted: 1 September 2020 doi:10.20944/preprints202009.0017.v1

dynamics is unable to estimate the temperature of bearings, therefore further studies are required to assess their temperature. Several papers have reported thermal modeling of bearings [37, 38]. Nevertheless, due to the relatively short duration of the testing procedure, the temperature variation of the bearing is not expected to exceed several °C, which results in the central wavelength shift that is at least by one order of magnitude smaller than the one caused by the bearing strain (considering typical FBG temperature sensitivity of approximately 10 pm/°C [39]). If the temperature influence is excluded from equation (10), then the function relating the shift of the central wavelength and deformation can be represented as follows:

$$f(\Delta\lambda_P) = c_3 \cdot \Delta\lambda_P^3 + c_2 \cdot \Delta\lambda_P^2 + c_1 \cdot \Delta\lambda_P + c_0, \quad (11)$$

where c_i are calibration coefficients. Applying equation (11) to the simulation and taking into account a typical gauge factor of FBGs equal to 1.2 picometers of wavelength shift per microstrain applied to the fiber [39], the central wavelength of the AFBS is calculated for five cases: without strain, at t = 6.35 s from the beginning of the maneuver, and at t = 6.8 s for both front left and front right bearings. The diagram showing the relative positions of the AFBS spectra and the filter with an inclined frequency response for the abovementioned cases is presented in Figure 10 (a).

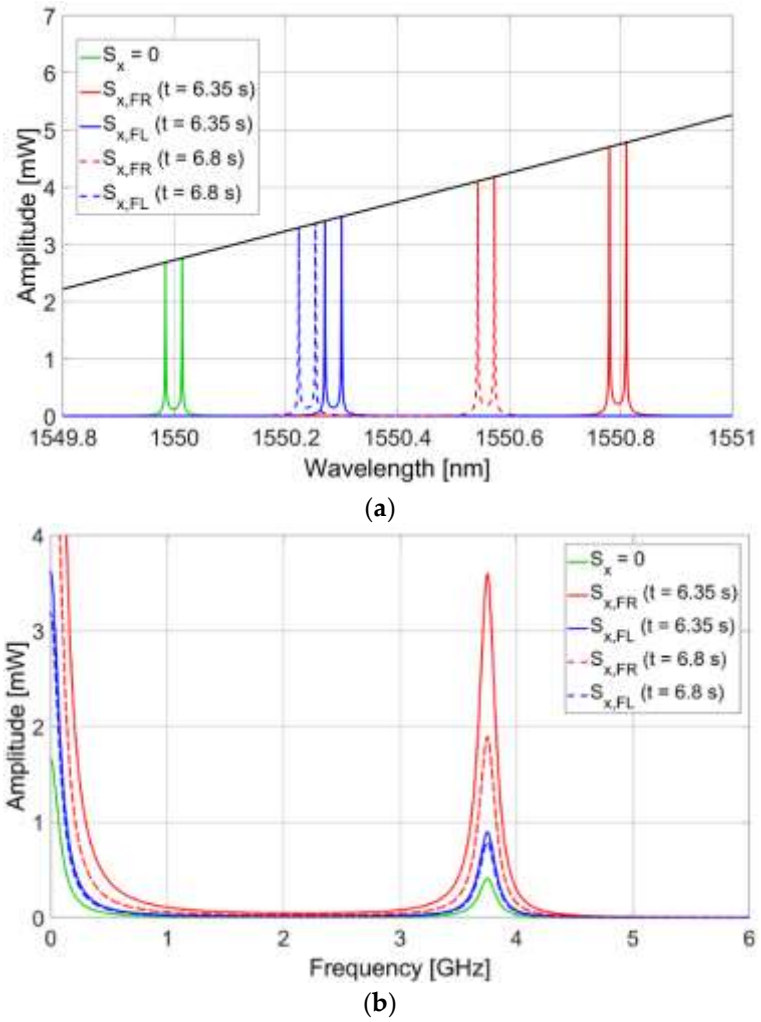

Figure 10. (**a**) AFBS spectra and the optical filter frequency response for five cases of applied strain: a spectrum of the AFBS without strain (green line), a spectrum for t = 6.35 s and t = 6.8 s of the front right bearing (red solid and dashed lines, respectively), a spectrum for t = 6.35 s and t = 6.8 s of the front left bearing (blue solid and dashed lines, respectively); (**b**) Corresponding spectra of electrical signal at the photodetector.

Preprints (www.preprints.org) | NOT PEER-REVIEWED | Posted: 1 September 2020 doi:10.20944/preprints202009.0017.v1

For each of the five cases of the AFBS central wavelength, the spectra of the electrical signal at the photodetector output were simulated. Figure 10 (b) presents the spectra for each corresponding case. As it is demonstrated in Figure 10 (b), the amplitude of the electric signal of the photodetector at the address frequency monotonically increases with the increase of the AFBS central wavelength shift.

7. Experimental Results

The prototype bearing depicted in Figure 11 (a) was instrumented with a single AFBS-sensor with the address frequency of 6.05 GHz. In order to ensure the uniformity of sensor strain and to eliminate lateral deformation of the sensor (since large lateral deformations applied to FBG impair the accuracy of the standard wavelength shift-strain relation of sensors [40]), a notch corresponding to the sensor length was made on the outer ring of the bearing. For preliminary testing, a static load was applied to the bearing by means of a mechanical press shown in Figure 11 (b), and the inner ring of the bearing was rotated using an electric screwdriver with the rotational speed of 360 rpm. The resulting amplitude of the measuring channel relative to the reference channel is presented in Figure 11 (c).

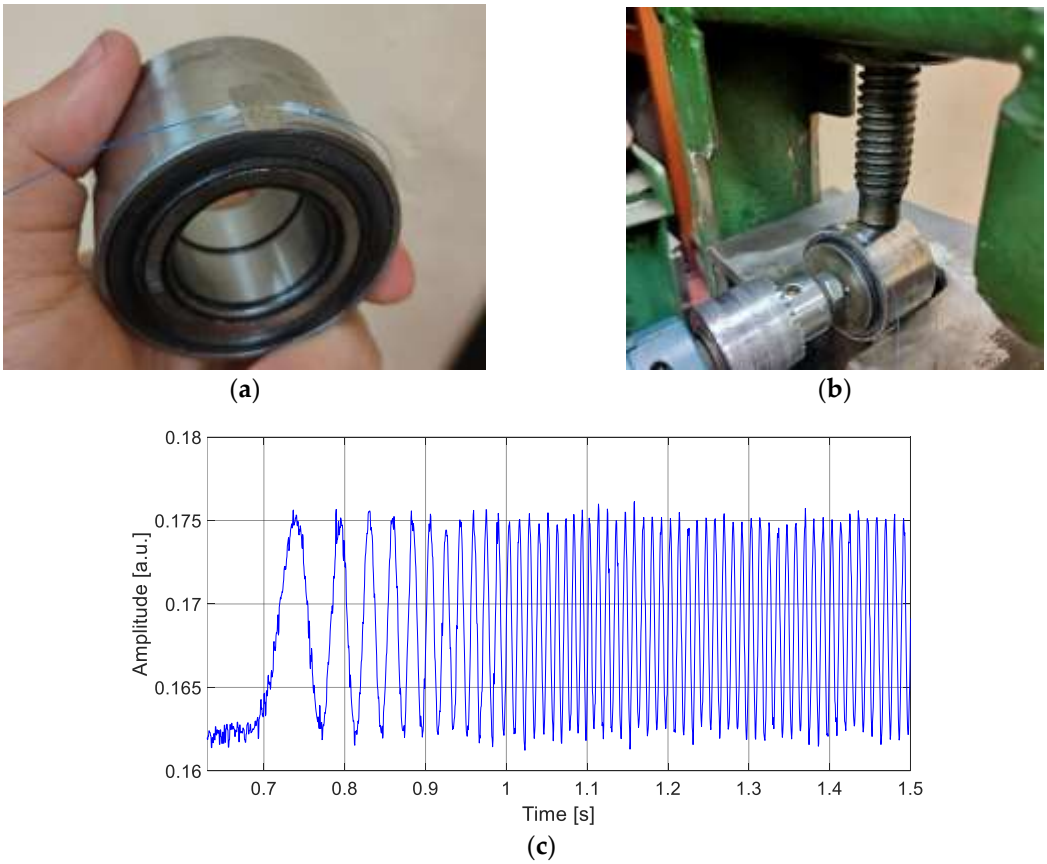

Figure 11. Static load test: (**a**) prototype load sensing bearing with AFBS sensor; (**b**) experimental setup with a mechanical press for static load test; (**c**) relative amplitude of the resulting beating signal at the photodetector during the static load test.

For the dynamic testing, the experimental setup included a B-class passenger vehicle with a prototype load sensing bearing installed in the modified front right wheel hub. The sprung mass of the testing vehicle was approximately 1200 kg, which is close to the one of the simulated vehicle.

The conditions of the split-mu braking test were unavailable at the time when experimental studies were carried out, therefore a straight-line braking to a standstill from the initial velocity of 30 km/h was chosen as a testing procedure. The testing was performed on a private driveway with dry asphalt pavement and air temperature of 21 °C.

 doi:10.20944/preprints202009.0017.v1

Figure 12 illustrates the results of tangential strain estimation for the whole duration of the testing maneuver. As it can be seen, the obtained experimental values are comparable with the simulation data. Higher experimental values of strain are mainly caused by higher road traction during the testing in comparison with the simulated conditions.

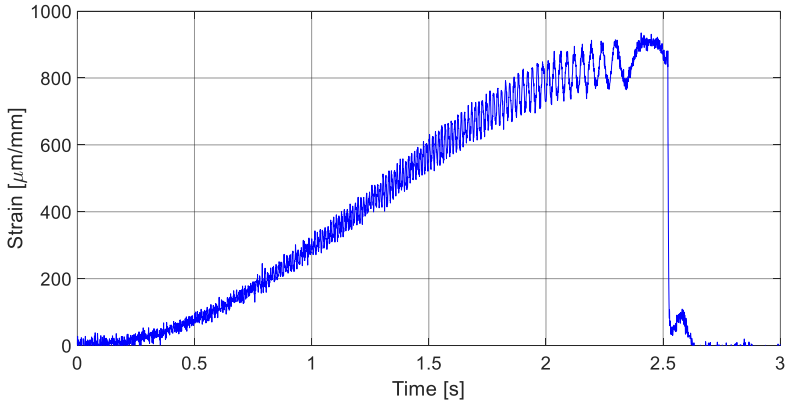

Figure 12. Tangential strain of the bearing measured by AFBS sensor for the whole duration of dynamic testing procedure.

The experimental results confirm the applicability of the proposed measurement approach for automotive load sensing bearings. Further studies are planned to increase the number of sensors used in the system for more comprehensive wheel forces measurement and temperature compensation.

8. Conclusions

The presented modeling approach demonstrated the feasibility of AFBS usage as sensing elements in load sensing bearings for automotive application. The two-frequency optical spectral response of AFBS results in a beating signal at the output of the photodetector, the amplitude of which can be used to explicitly define the central wavelength shift of the AFBS sensor. According to the simulation results, the estimation error of the longitudinal wheel force from the strain data acquired by a single sensor was 5.44% with root-mean-square error of 113.64 N. The experimental results of the strain measurement are fully comparable with the simulation data. Further research will be conducted with an increased number of sensors providing measurement of wheel forces in various directions as well as ensuing temperature compensation for prolonged testing procedures.

Author Contributions: Conceptualization, T.A., O.M. and V.I.; methodology, A.S. and A.K.; software, R.G.; validation, T.A., R.G. and A.K.; formal analysis, A.S.; investigation, T.A. and R.G.; resources, R.G.; data curation, A.S.; writing—original draft preparation, T.A.; writing—review and editing, A.S., O.M. and V.I.; visualization, R.G.; supervision, O.M.; project administration, A.S.; funding acquisition, O.M. and A.K. All authors have read and agreed to the published version of the manuscript.

Funding: T.A., R.G., A.S. and O.M. were funded by Ministry of Science and Higher Education of the Russian Federation (Agreement No. 075-03-2020-051, topic No. fzsu-2020-0020), A.K. was funded by Grant from the President of the Russian Federation for state support of young Russian scientists – candidates of sciences MK-3421.2019.8 (agreement No. 075-15-2019-309).

References

1. Pretagostini, F.; Ferranti, L.; Berardo, G.; Ivanov, V.; Shyrokau, B. Survey on Wheel Slip Control Design Strategies, Evaluation and Application to Antilock Braking Systems, *IEEE Access* **2020**, *8*, 10951-10970. DOI: 10.1109/ACCESS.2020.2965644.
2. Aksjonov, A.; Augsburg, K.; Vodovozov, V. Design and Simulation of the Robust ABS and ESP Fuzzy Logic Controller on the Complex Braking Maneuvers. *Applied Sciences* **2016**, *6*, 382. DOI: 10.3390/app6120382

3. Viehweger, M; Vaseur, C.; van Aalst, S. et al. Vehicle State and Tyre Force Estimation: Demonstrations and Gudelines. *Vehicle System Dynamics* **2020**, *232(14)*, 1883–1930. DOI: 10.1080/00423114.2020.1714672.
4. Canudas-de-Wit, C.; Tsiotras, P.; Efstathios, V.; Michel, B.; Gissinger, G.l. Dynamic Friction Models for Road/Tire Longitudinal Interaction. *Vehicle System Dynamics* **2003**, *39*, 189-226. DOI: 10.1076/vesd.39.3.189.14152
5. Jousimaa, O.J.; Xiong, Y.; Niskanen, A.J.; Tuononen, A.J. Energy harvesting system for intelligent tyre sensors, Proceedings of the 2016 IEEE Intelligent Vehicles Symposium (IV), Gothenburg, Sweden, 19–22 June 2016. DOI: 10.1109/IVS.2016.7535445
6. Hopping, K.; Augsburg, K.; Buchner, F. Extending the HSRI tyre model for large inflation pressure changes, Conference: Engineering for a Changing World: 59th IWK, Ilmenau Scientific Colloquium, Technische Universität Ilmenau, Ilmenau, Germany, 11–15 September 2017.
7. Vehicle dynamics, durability and tire testing. Kistler Group (2020). Available online: https://www.kistler.com/en/applications/automotive-research-test/vehicle-dynamics-durability/tire-testing/ (accessed on 24 August 2020).
8. Coppo, F.; Pepe, G.; Roveri, N.; Carcaterra, A. A Multisensing Setup for the Intelligent Tire Monitoring. *Sensors* **2017**, *17 (3)*, 00576. DOI: 10.3390/s17030576
9. Carcaterra, A.; Roveri, N.; Gianluca, P. OPTYRE – A new technology for tire monitoring: Evidence of contact patch phenomena. *Mechanical Systems and Signal Processing* **2015**, *66-67*, 793-810. DOI: 10.1016/j.ymssp.2015.06.019
10. Roveri, N.; Pepe, G.; Mezzani, F.; Carcaterra, A.; Culla, A.; Milana, S. OPTYRE—Real Time Estimation of Rolling Resistance for Intelligent Tyres. *Sensors* **2019**, *19*, 5119. DOI: 10.3390/s19235119
11. Xiong, Y.; Juhani, A. A multi-laser sensor system to measure rolling deformation for truck tyres. *Vehicle Performance* **2017**, *3(2)*, 115-126. DOI: 10.1504/IJVP.2017.10003355
12. Xiong, Y.; Juhani, A. Rolling deformation of truck tires: Measurement and analysis using a tire sensing approach. *Journal of Terramechanics* **2015**, *61*, 33-42. DOI: 10.1016/j.jterra.2015.07.004
13. Matsuzaki, R.; Hiraoka, N.; Todoroki, A.; Mizutani, Y. Strain Monitoring and Applied Load Estimation for the Development of Intelligent Tires Using a Single Wireless CCD Camera. *J. Solid Mech. Mater. Eng.* **2012**, *6*, 935–949. DOI: 10.1299/jmmp.6.935
14. Mendoza-Petit, M.F.; Garcia-Pozuelo, D.; Olatunbosun, O.A. A Strain-Based Method to Estimate Tire Parameters for Intelligent Tires under Complex Maneuvering Operations. *Sensors* **2019**, *19*, 2973. DOI: 10.3390/s19132973
15. Mendoza-Petit, MF.; Garcia-Pozuelo, D.; Díaz, V.; Olatunbosun, O.A. A Strain-Based Intelligent Tire to Detect Contact Patch Features for Complex Maneuvers. *Sensors* **2020**, *20*, 1750. DOI: 10.3390/s20061750
16. Singh, K.B.; Taheri, S. Accelerometer Based Method for Tire Load and Slip Angle Estimation. *Vibration* **2019**, *2*, 174-186. DOI: 10.3390/vibration2020011
17. Suzuki, M.; Nakano, K.; Miyoshi, A.; Katagiri, A.; Kunii, M. Method for Sensing Tire Force in Three Directional Components and Vehicle Control Using This Method. *SAE Technical Paper 2007-01-0830* **2007**. DOI:10.4271/2007-01-0830.
18. Ohkubo, N.; Horiuchi, T.; Yamamoto, O.; Inagaki, H. Brake Torque Sensing for Enhancement of Vehicle Dynamics Control Systems. *SAE Technical Paper 2007-01-0867* **2007**. DOI:10.4271/2007-01-0867.
19. Den Engelse, J. Estimation of the Lateral Force, Acting at the Tire Contact Patch of a Vehicle Wheel, Using a Hub Bearing Unit Instrumented With Strain Gauges and Eddy-current Sensors. MSc Thesis, Delft University of Technology, Delft, 2013.
20. Kerst, S; Shyrokau, B; Holweg, E. Reconstruction of Wheel Forces Using an Intelligent Bearing, *SAE Int. J. of Passenger Cars – Mechanical Systems* **2016**, 9(1), 196–203. DOI: 10.4271/2016-01-0092.
21. Nishikawa, K. Hub Bearing with Integrated Multi-axis Load Sensor. *Technical Review* **2011**, *79*, 58-63.
22. Kerst, S; Shyrokau, B; Holweg, E. A model-based approach for the estimation of bearing forces and moments using outer-ring deformation. *IEEE Transactions on Industrial Electronics* **2019**, 67(1), 461-470. DOI: 10.1109/TIE.2019.2897510.
23. Dincmen, E.; Güvenç, B.A.; Acarman, T. Extremum-Seeking Control of ABS Braking in Road Vehicles With Lateral Force Improvement. *IEEE Transactions on Control Systems Technology* **2014**, *22*, 230-237. DOI: 10.1109/TCST.2012.2229465
24. Gandhi, N. Load Estimation and Uncertainty Analysis Based on Strain Measurement: With Application to Load Sensing Bearing. MSc. Thesis, Delft University of Technology, Delft, 2013.

25. Oswald, F.B.; Zaretsky, E.V.; Poplawski, J.V. Effect of Internal Clearance on Load Distribution and Life of Radially Loaded Ball and Roller Bearings. *Tribology Transactions* **2012**, *55*, 245-265. DOI: 10.1080/10402004.2011.639050.
26. Sakhabutdinov, A.Zh.; Morozov, O.G.; Morozov, G.A. Universal Microwave Photonics Approach to Frequency-Coded Quantum Key Distribution. In *Advanced Technologies of Quantum Key Distribution*; Gnatyuk, S. IntechOpen: London, UK, 2018. DOI: 10.5772/intechopen.71974
27. Agliullin, T.A.; Gubaidullin, R.R.; Ivanov, V.; Morozov, O.G.; Sakhabutdinov, A.Zh. Addressed FBG-structures for tire strain measurement. Proc. SPIE 11146, Optical Technologies for Telecommunications 2018, Ufa, Russian Federation, 20-22 November 2018, 111461E. DOI: 10.1117/12.2523849
28. Gubaidullin, R.R.; Agliullin, T.A.; Morozov, O.G.; Sahabutdinov, A.Z.; Ivanov, V. Microwave-Photonic Sensory Tire Control System Based on FBG. Proceedings of 2019 Systems of Signals Generating and Processing in the Field of on Board Communications, Moscow, Russia, 20-21 March 2019. DOI: 10.1109/SOSG.2019.8706790
29. Morozov, O.G.; Sakhabutdinov, A.J. Addressed fiber Bragg structures in quasidistributed microwave-photonic sensor systems. *Computer Optics* **2019**, *43(4)*, 535-543. DOI: 10.18287/2412-6179-2019-43-4-535-543
30. Morozov, O.G.; Sakhabutdinov, A.Zh.; Nureev. I.I.; Misbakhov, R.Sh. Modelling and record technologies of address fibre Bragg structures based on gratings with two symmetrical pi-phase shifts. *J. Phys.: Conf. Ser*. **2019**, *1368*, 022048. DOI: 10.1088/1742-6596/1368/2/022048
31. Agliullin, T.A.; Kurbiev, I.U.; Gubaidullin, R.R.; Morozov. O.G.; Ivanov, V. Load Sensing Bearings for Automotive Applications Based on Addressed Fiber Bragg Structures. Proceedings of 2019 Systems of Signal Synchronization, Generating and Processing in Telecommunications (SYNCHROINFO), Yaroslavl, Russia, 1-3 July 2019. DOI: 10.1109/SYNCHROINFO.2019.8814178
32. Gubaidullin, R.R.; Sahabutdinov, A.Z.; Agliullin, T.A.; Morozov. O.G.; Ivanov, V. Application of Addressed Fiber Bragg Structures for Measuring Tire Deformation. Proceedings of 2019 Systems of Signal Synchronization, Generating and Processing in Telecommunications (SYNCHROINFO), Yaroslavl, Russia, 1-3 July 2019. DOI: 10.1109/SYNCHROINFO.2019.8813908
33. Gubaidullin, R.R.; Agliullin, T.A.; Nureev, I.I.; Sahabutdinov, A.Z.; Ivanov, V. Application of Gaussian Function for Modeling Two-Frequency Radiation from Addressed FBG. Proceedings of 2020 Systems of Signals Generating and Processing in the Field of on Board Communications, Moscow, Russia, 19-20 March 2020. DOI: 10.1109/IEEECONF48371.2020.9078587
34. Sahabutdinov, A.Z.; Morozov, O.G.; Agliullin, T.A.; Gubaidullin. R.R.; Ivanov, V. Modeling of Spectrum Response of Addressed FBG-Structures in Load Sensing Bearings. Proceedings of 2020 Systems of Signals Generating and Processing in the Field of on Board Communications, Moscow, Russia, 19-20 March 2020. DOI: 10.1109/IEEECONF48371.2020.9078659.
35. Morozov, O.; Sakhabutdinov, A.; Anfinogentov, V.; Misbakhov, R.; Kuznetsov, A.; Agliullin, T. Multi-Addressed Fiber Bragg Structures for Microwave-Photonic Sensor Systems. *Sensors* **2020**, *20*, 2693. DOI: 10.3390/s20092693
36. Sakhabutdinov, A.Zh.; Nureev, I.I.; Morozov, O.G.; Kuznetsov, A.A.; Faskhutdinov, L.M.; Petrov, A.V.; Kuchev, S.M. Calibration of combined pressure and temperature sensors. *International Journal of Applied Engineering Research* **2015**, *10(24)*, 44948-44957.
37. Gupta, P.K.; Taketa, J.I.; Price, C.M. Thermal interactions in rolling bearings. *Proceedings of the Institution of Mechanical Engineers, Part J: Journal of Engineering Tribology* **2019**, *234(8)*, 1233–1253. DOI: 10.1177/1350650119886234
38. Kumaran, S.S.; Velmurugan, P.; Tilahun, S. Effect on stress and thermal analysis of tapered roller bearings. *Journal of Critical Reviews* **2020**, *7(9)*, 492-501. DOI: 10.31838/jcr.07.09.99
39. Fajkus, M.; Nedoma, J.; Martinek, R.; Vasinek, V.; Nazeran, H.; Siska, P. A Non-Invasive Multichannel Hybrid Fiber-Optic Sensor System for Vital Sign Monitoring. *Sensors* **2017**, *17*, 111. DOI: 10.3390/s17010111
40. Lai, M.; Karalekas, D.; Botsis, J. On the Effects of the Lateral Strains on the Fiber Bragg Grating Response. *Sensors* **2013**, *13*, 2631-2644. DOI: 10.3390/s130202631